PAPER

Check for updates

Structure and magnetism of the Rh^{4+}-containing perovskite oxides $La_{0.5}Sr_{0.5}Mn_{0.5}Rh_{0.5}O_3$ and $La_{0.5}Sr_{0.5}Fe_{0.5}Rh_{0.5}O_3$†

Nijat Hasanli,[a] Alex Scrimshire,[b] Paul A. Bingham,[b] Robert G. Palgrave [iD][c] and Michael A. Hayward [iD] *[a]

Synchrotron X-ray powder diffraction data indicate that $La_{0.5}Sr_{0.5}Mn_{0.5}Rh_{0.5}O_3$ and $La_{0.5}Sr_{0.5}Fe_{0.5}Rh_{0.5}O_3$ adopt distorted perovskite structures (space group *Pnma*) with *A*-site and *B*-site cation disorder. A combination of XPS and ^{57}Fe Mössbauer data indicate the transition metal cations in the two phases adopt Mn^{3+}/Rh^{4+} and Fe^{3+}/Rh^{4+} oxidation state combinations respectively. Transport data indicate both phases are insulating, with ρ *vs.* T dependences consistent with 3D variable-range hopping. Magnetisation data reveal that $La_{0.5}Sr_{0.5}Mn_{0.5}Rh_{0.5}O_3$ adopts a ferromagnetic state below $T_c \sim 60$ K, which is rationalized on the basis of coupling *via* a dynamic Jahn–Teller distortion mechanism. In contrast, magnetic data reveal $La_{0.5}Sr_{0.5}Fe_{0.5}Rh_{0.5}O_3$ undergoes a transition to a spin-glass state at $T \sim 45$ K, attributed to frustration between nearest-neighbour Fe–Rh and next-nearest-neighbour Fe–Fe couplings.

Introduction

Transition-metal oxides which adopt the ABO_3 perovskite structure exhibit a wide variety of complex physical properties, including superconductivity, colossal magnetoresistance, ferroelectricity and a wide variety of other coupled electronic and magnetic behaviours.[1] The rich diversity of electronic and magnetic phenomena displayed by perovskite oxides can be attributed to the strong coupling between the local electronic states of the octahedrally coordinated transition-metal cations, which is facilitated by strong covalency in the *B*–O–*B* links which connect the BO_6 units.[2]

Recently there has been much interest in perovskite oxide compounds which combine 3d and 4d or 3d and 5d transition-metal cations, because the contrasting features of the 3d (narrow metal d-bands, large on-site electron–electron repulsion) and 4d/5d (broad d-bands, low on-site repulsion, strong spin–orbit coupling for 5d) cations can result in novel behaviour when they are combined.[3,4] For example, Sr_2FeMoO_6 exhibits half-metallic ferromagnetic behaviour attributed to the interaction between the localized $3d^5$ electronic configuration of Fe^{3+} and the delocalized $4d^1$ electrons of Mo^{5+},[5] with similar behaviour observed in other 3d/4d and 3d/5d systems.[6,7]

In a broader context the inter-cation magnetic couplings in mixed 3d/4d and 3d/5d perovskite oxides do not generally appear to follow the Goodenough Kanamouri rules[8] which dominate 3d systems.[9–11] However, to date only a subset of the 3d/4d and 3d/5d perovskite oxide phases which could be envisioned have been reported,[12] so it is hard to formulate broad magnetic coupling rules for this class of compound. To help address this situation, we have been studying mixed perovskite phases containing rhodium.

A range of Rh-containing perovskite oxides of the form $LaM_{0.5}Rh_{0.5}O_3$ have been reported (M = Cr, Mn, Fe, Co, Ni and Cu) with M/Rh cation disordered structures.[13–16] The unit cell volumes of these $LaM_{0.5}Rh_{0.5}O_3$ compounds are broadly consistent with an M^{3+}/Rh^{3+} oxidation state combination, with the exception of $LaCu_{0.5}Rh_{0.5}O_3$ which appears to adopt a configuration close to a Cu^{2+}/Rh^{4+} combination.[13,15] However, Curie constants obtained by fitting the Curie–Weiss law to temperature-dependent magnetization data deviate from values expected for combinations of M^{3+} and low-spin, $S = 0$ Rh^{3+}, casting some doubt on this oxidation state assignment.[13] In the case of $LaCo_{0.5}Rh_{0.5}O_3$ the deviations are large and temperature dependent and have been attributed to both a change in the spin-state of Co^{3+} and the presence of Co^{2+}/Rh^{4+} oxidation state combinations.[17–19]

Here we report two further cation-disordered rhodium-containing perovskite oxides, $La_{0.5}Sr_{0.5}Mn_{0.5}Rh_{0.5}O_3$ and

[a]Department of Chemistry, University of Oxford, Inorganic Chemistry Laboratory, South Parks Road, Oxford, OX1 3QR, UK. E-mail: michael.hayward@chem.ox.ac.uk
[b]Materials and Engineering Research Institute, Sheffield Hallam University, City Campus, Howard Street, Sheffield, S1 1WB, UK
[c]Department of Chemistry, Department of Chemistry, University College London, 20 Gordon Street, London, WC1H 0AJ, UK
†Electronic supplementary information (ESI) available: Mn 2P and Fe 2P XPS from $La_{0.5}Sr_{0.5}Mn_{0.5}Rh_{0.5}O_3$ and $La_{0.5}Sr_{0.5}Fe_{0.5}Rh_{0.5}O_3$ respectively; additional fits to ^{57}Fe Mössbauer data from $La_{0.5}Sr_{0.5}Fe_{0.5}Rh_{0.5}O_3$. See DOI: 10.1039/d0dt02466j

$La_{0.5}Sr_{0.5}Fe_{0.5}Rh_{0.5}O_3$. Using a combination of XPS and ^{57}Fe Mössbauer spectroscopy we demonstrate that, even though these compounds were prepared at ambient pressure, the rhodium cations adopt an Rh^{4+} oxidation state, resulting in ferromagnetic behaviour for $La_{0.5}Sr_{0.5}Mn_{0.5}Rh_{0.5}O_3$ and spin-glass behaviour for $La_{0.5}Sr_{0.5}Fe_{0.5}Rh_{0.5}O_3$.

Experimental

Synthesis

Samples of $La_{0.5}Sr_{0.5}Mn_{0.5}Rh_{0.5}O_3$ and $La_{0.5}Sr_{0.5}Fe_{0.5}Rh_{0.5}O_3$ were prepared via a high-temperature ceramic route. Suitable quantities of La_2O_3 (99.999%, dried at 900 °C) $SrCO_3$ (99.994%), Rh_2O_3 (99.99%, dried at 800 °C) and either MnO_2 (99.997%) or Fe_2O_3 (99.997%) were ground together in an agate pestle and mortar and then heated in air to 1000 °C in an alumina crucible. The resulting powders were then reground and pressed into pellets. Samples of $La_{0.5}Sr_{0.5}Mn_{0.5}Rh_{0.5}O_3$ were then heated in air at 1300 °C for 4 periods of 48 h. Samples of $La_{0.5}Sr_{0.5}Fe_{0.5}Rh_{0.5}O_3$ were heated under flowing oxygen at 1300 °C for 3 periods of 48 h. All samples were reground and pressed into pellets between heating periods.

Characterization

X-ray powder diffraction data were collected using a PANalytical X'pert diffractometer incorporating an X'celerator position-sensitive detector (monochromatic Cu Kα_1 radiation). High-resolution synchrotron X-ray powder diffraction data (SXRD) were collected using the I11 instrument at the Diamond Light Source Ltd. Diffraction patterns were collected using Si-calibrated X-rays with an approximate wavelength of 0.825 Å from samples sealed in 0.3 mm diameter borosilicate glass capillaries. Rietveld refinements were performed using the GSAS suite of programs.[20] Magnetization data were collected using a Quantum Design MPMS SQUID magnetometer. Four-probe resistivity measurements were performed using a home-made apparatus on bars cut from sintered pellets. ^{57}Fe Mössbauer spectroscopy measurements utilized acrylic absorber discs with a sample area of 1.767 cm^2 which were loaded to present 2.16×10^{-3} g cm^{-2} of Fe, and achieve a Mössbauer thickness of 1. Samples were homogeneously mixed with graphite to achieve this level of loading. The 14.4 keV γ-rays were supplied by the cascade decay of 25 mCi ^{57}Co in a Rh matrix source, oscillated at constant acceleration by a SeeCo W304 drive unit, and detected using a SeeCo 45431 Kr proportional counter operating with 1.745 kV bias voltage applied to the cathode. All measurements were calibrated relative to α-Fe foil. Spectral data were fitted using the Recoil software package,[21] using Lorentzian line shapes.

X-ray photoelectron spectroscopy (XPS) analysis was performed using a Kratos Axis SUPRA XPS fitted with a monochromated Al K$_\alpha$ X-ray source (1486.7 eV), a spherical sector analyser and 3 multichannel resistive plate, 128 channel delay line detectors. All data was recorded at 150 W and a spot size of

700×300 μm. Survey scans were recorded at a pass energy of 160 eV, and high-resolution scans recorded at a pass energy of 20 eV. Electronic charge neutralization was achieved using a magnetic immersion lens. Filament current = 0.27 A, charge balance = 3.3 V, filament bias = 3.8 V. All sample data was recorded at a pressure below 10^{-8} Torr and a room temperature of 294 K. Data was analysed using CasaXPS v2.3.18PR1.0. C 1s sp^3 peaks were calibrated to 284.8 eV.

Results

Structural characterisation of $La_{0.5}Sr_{0.5}Mn_{0.5}Rh_{0.5}O_3$

SXRD data collected from $La_{0.5}Sr_{0.5}Mn_{0.5}Rh_{0.5}O_3$ at room temperature could be readily indexed using an orthorhombic unit cell (a = 5.483 Å, b = 7.776 Å, 5.536 Å) with extinction conditions consistent with the $Pnma$ (# 62) space group. A structural model was constructed based on the reported structure of $LaMn_{0.5}Rh_{0.5}O_3$,[15] but with the La^{3+} replaced by a 1 : 1 ratio of La^{3+} : Sr^{2+}. This model was refined against the SXRD data to achieve a good fit as shown in Fig. 1 and detailed in Table 1, with selected bond lengths listed in Table 2. SXRD data provide no evidence for Mn/Rh cation-order, with a model based on the reported cation-ordered structure of $LaSrNiRuO_6$ (space group $P2_1/n$)[11] reverting to a disordered structure when the Mn and Rh occupancies were refined.

Structural and chemical characterisation of $La_{0.5}Sr_{0.5}Fe_{0.5}Rh_{0.5}O_3$

SXRD data collected from $La_{0.5}Sr_{0.5}Fe_{0.5}Rh_{0.5}O_3$ at room temperature could be readily indexed using an orthorhombic unit cell (a = 5.525 Å, b = 7.860 Å, 5.563 Å,) with extinction conditions consistent with the $Pnma$ (# 62) space group. A structural model was constructed, based that used for $La_{0.5}Sr_{0.5}Mn_{0.5}Rh_{0.5}O_3$, and refined against the SXRD data to achieve a good fit as shown in Fig. 2 and detailed in Table 3, with selected bond lengths listed in Table 4. SXRD data
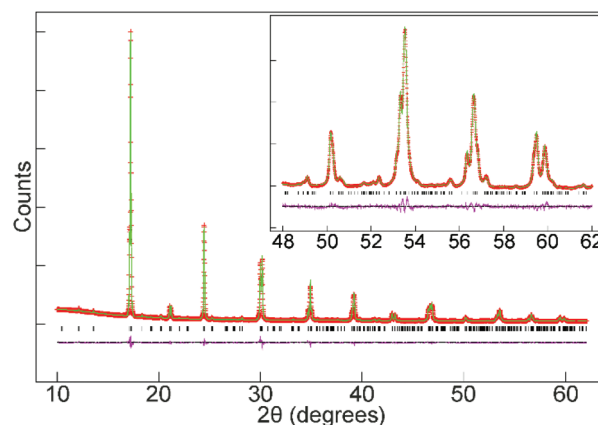
Fig. 1 Observed, calculated and difference plots from the structural refinement of $La_{0.5}Sr_{0.5}Mn_{0.5}Rh_{0.5}O_3$ against SXRD data collected at room temperature. Inset shows quality of fit at large values of 2θ.
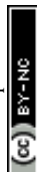
Table 1 Parameters from the structural refinement of $La_{0.5}Sr_{0.5}Mn_{0.5}Rh_{0.5}O_3$ against synchrotron X-ray powder diffraction data

Atom	x	y	z	Occupancy	U_{iso} (Å^2)
La/Sr	0.5181(1)	$\frac{1}{4}$	0.0023(1)	0.5/0.5	0.009(1)
Mn/Rh	0	0	0	0.5/0.5	0.004(1)
O(1)	0.0000(6)	$\frac{1}{4}$	0.9434(6)	1	0.009(1)
O(2)	0.2701(8)	0.0305(4)	0.2189(6)	1	0.020(1)

$La_{0.5}Sr_{0.5}Mn_{0.5}Rh_{0.5}O_3$ space group *Pnma* (#62). a = 5.4830(1) Å, b = 7.7769(1) Å, 5.5364(1) Å, volume = 236.08(1). Formula mass: 240.18 g mol^{-1}, Z = 4. Radiation source: Synchrotron X-ray, λ = 0.82622 Å. χ^2 = 19.75; wR_p = 2.92%; R_p = 1.88%.

Table 2 Selected bond lengths from the structure of $La_{0.5}Sr_{0.5}Mn_{0.5}Rh_{0.5}O_3$

| Cation	Anion	Bond length (Å)
Mn/Rh	O(1) × 2	1.969(1)
	O(2) × 2	1.928(4)
	O(2) × 2	2.017(4)
La/Sr	O(1)	2.470(3)
	O(1)	2.662(3)
	O(1)	2.859(3)
	O(1)	3.070(3)
	O(2) × 2	2.490(4)
	O(2) × 2	2.684(4)
	O(2) × 2	2.758(3)
	O(2) × 2	3.117(4)

Table 3 Parameters from the structural refinement of $La_{0.5}Sr_{0.5}Fe_{0.5}Rh_{0.5}O_3$ against synchrotron X-ray powder diffraction data

Atom	x	y	z	Occupancy	U_{iso} (Å^2)
La/Sr	0.5138(3)	$\frac{1}{4}$	0.0012(6)	0.5/0.5	0.007(1)
Fe/Rh	0	0	0	0.5/0.5	0.003(1)
O(1)	0.9982(5)	$\frac{1}{4}$	0.0369(4)	1	0.009(1)
O(2)	0.2294(3)	0.9594(1)	0.2800(2)	1	0.016(1)

$La_{0.5}Sr_{0.5}Fe_{0.5}Rh_{0.5}O_3$ space group *Pnma* (#62). a = 5.5254(3) Å, b = 7.8602(5) Å, 5.5635(4) Å, volume = 241.63(3). Formula mass: 240.63 g mol^{-1}, Z = 4. Radiation source: Synchrotron X-ray, λ = 0.8259 Å. χ^2 = 15.85; wR_p = 2.41%; R_p = 1.54%.

Table 4 Selected bond lengths from the structure of $La_{0.5}Sr_{0.5}Fe_{0.5}Rh_{0.5}O_3$

Cation	Anion	Bond (Å)
Fe/Rh	O(1) × 2	1.976(1)
	O(2) × 2	1.958(1)
	O(2) × 2	2.033(1)
La/Sr	O(1)	2.571(4)
	O(1)	2.684(3)
	O(1)	2.856(3)
	O(1)	2.995(4)
	O(2) × 2	2.456(2)
	O(2) × 2	2.678(2)
	O(2) × 2	2.849(2)
	O(2) × 2	3.176(2)
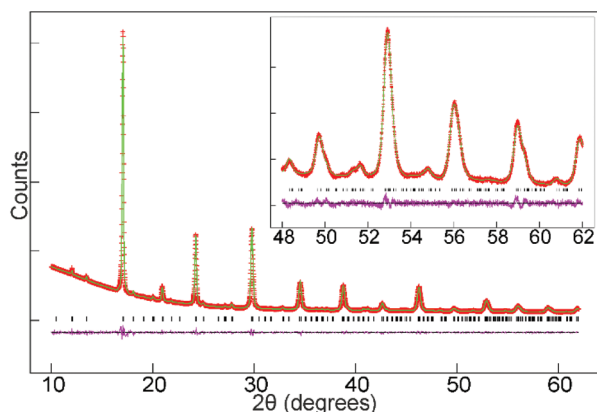
Fig. 2 Observed, calculated and difference plots from the structural refinement of $La_{0.5}Sr_{0.5}Fe_{0.5}Rh_{0.5}O_3$ against SXRD data collected at room temperature. Inset shows quality of fit at large values of 2θ.

Fig. 3 ^{57}Fe Mössbauer spectrum collected from $La_{0.5}Sr_{0.5}Fe_{0.5}Rh_{0.5}O_3$ at room temperature.

provide no evidence for Fe/Rh cation-order, with a model based on the reported cation-ordered structure of $LaSrNiRuO_6$ (space group $P2_1/n$)[11] reverting to a disordered structure when the Fe and Rh occupancies were refined.

^{57}Fe Mössbauer analysis of $La_{0.5}Sr_{0.5}Fe_{0.5}Rh_{0.5}O_3$

A ^{57}Fe Mössbauer spectrum collected from $La_{0.5}Sr_{0.5}Fe_{0.5}Rh_{0.5}O_3$ at room temperature can be satisfactorily fitted by two doublets as shown in Fig. 3 and detailed in Table 5.
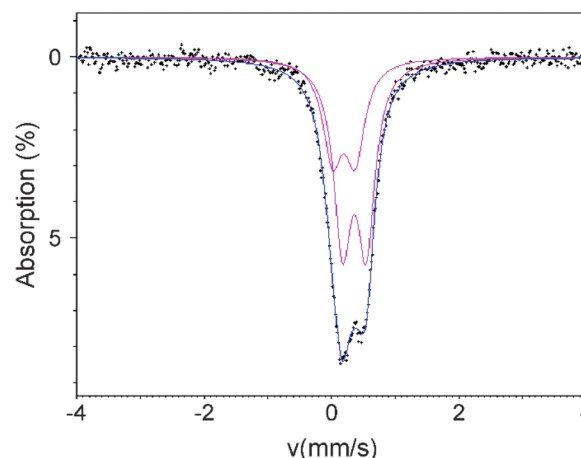
Table 5 Parameters extracted from fit to ^{57}Fe Mössbauer spectrum collected from $La_{0.5}Sr_{0.5}Fe_{0.5}Rh_{0.5}O_3$ (χ^2 = 0.650)

Doublet	C_S (mm s^{-1})	Δ (mm s^{-1})	HWHM (mm s^{-1})	Site population (%)
1	0.361(18)	0.371(6)	0.166(16)	63(19)
2	0.195(42)	0.355(14)	0.184(24)	37(19)

We attribute the need to use two doublets to obtain a satisfactory fit to the Fe/Rh cation-disordered structure of $La_{0.5}Sr_{0.5}Fe_{0.5}Rh_{0.5}O_3$. Each octahedral transition-metal coordination site in the perovskite framework is surrounded by 6 others. In a disordered Fe/Rh array the majority of the iron cations with have 3 iron neighbours and 3 rhodium neighbours. However there will be a significant number which have Fe_2Rh_4 or Fe_4Rh_2 surrounding them and a smaller number with Fe_1Rh_5 or Fe_5Rh_1. When we also consider that the Fe_3Rh_3 environments can be arranged as either *fac* or *mer*, and the Fe_2Rh_4 and Fe_4Rh_2 as *cis* or *trans*, it can be seen that there are a large number of local environments for the iron cations within the disordered Rh/Fe array, each with a different Mössbauer chemical shift and doublet splitting. It is not possible to resolve this large number of components from the data in a meaningful way, so we have utilized a 2-doublet fit to extract the range of C_s and Δ values spanned by the different Fe local coordination environments. Comparison with literature standards indicates these signals correspond to octahedrally coordinated Fe^{3+}.[22,23]

To investigate the possibility that some Fe^{4+} cations are present in $La_{0.5}Sr_{0.5}Fe_{0.5}Rh_{0.5}O_3$ we have performed a further fit in which one doublet was fixed at $C_S = 0$, corresponding to Fe^{4+}. This approach also gives a reasonable fit to the data and indicates a maximum concentration of 12(2)% Fe^{4+} as described in detail in the ESI.†

XPS analysis of $La_{0.5}Sr_{0.5}Mn_{0.5}Rh_{0.5}O_3$ and $La_{0.5}Sr_{0.5}Fe_{0.5}Rh_{0.5}O_3$

A Rh 3d spectrum collected from $La_{0.5}Sr_{0.5}Fe_{0.5}Rh_{0.5}O_3$ is shown in Fig. 4a and exhibits a well resolved Rh $3d_{5/2}$ component centred at BE = 308.9 eV (FWHM = 1.86 eV) and a Rh $3d_{3/2}$ component centred at BE = 313.7 eV (FWHM = 2.63 eV). When combined with an O 1s–Rh $3d_{5/2}$ separation of 219.6 eV, as shown in Fig. 4a, these values indicate an oxidation state of Rh^{4+}.[24,25] Fe 2p spectra (Fig. S2, ESI†) exhibit a well resolved Fe $2p_{3/2}$ component centred at BE = 710.1 eV (FWHM = 3.44 eV) and a Fe $2p_{1/2}$ component centred at BE = 723.3 eV (FWHM = 4.65 eV), consistent with Fe^{3+}.[26,27] These data, in combination with the ^{57}Fe Mössbauer data indicate an Fe^{3+}/Rh^{4+} oxidation state combination for $La_{0.5}Sr_{0.5}Fe_{0.5}Rh_{0.5}O_3$.

Similarly, a Rh 3d spectrum collected from $La_{0.5}Sr_{0.5}Mn_{0.5}Rh_{0.5}O_3$, shown in Fig. 4b, exhibits a well resolved Rh $3d_{5/2}$ component centred at BE = 308.7 eV (FWHM = 1.45 eV), a Rh $3d_{3/2}$ component centred at BE = 313.4 eV (FWHM = 2.16 eV) and a O 1s–Rh $3d_{5/2}$ separation of 220.0 eV which also indicate an oxidation state of Rh^{4+}.[24,25] Mn 2p spectra (Fig. S3, ESI†) exhibit a well resolved Mn $2p_{3/2}$ component centred at BE = 641.6 eV (FWHM = 3.79 eV) and a Mn $2p_{1/2}$ component centred at BE = 652.9 eV (FWHM = 4.35 eV), consistent with Mn^{3+}.[26,28] These data indicate an Mn^{3+}/Rh^{4+} oxidation state combination for $La_{0.5}Sr_{0.5}Mn_{0.5}Rh_{0.5}O_3$.

Magnetic characterisation of $La_{0.5}Sr_{0.5}Mn_{0.5}Rh_{0.5}O_3$

Zero-field cooled (ZFC) and field cooled (FC) magnetization data collected from $La_{0.5}Sr_{0.5}Mn_{0.5}Rh_{0.5}O_3$ in an applied field
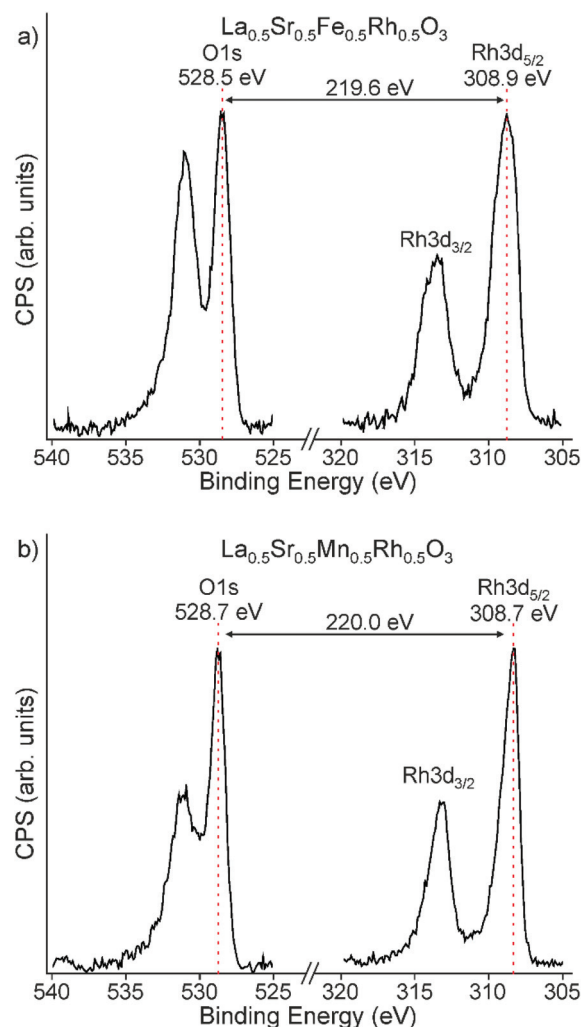

Fig. 4 Binding energy separation between O 1s and Rh 3d peaks of (a) $LaSrFe_{0.5}Rh_{0.5}O_3$ and (b) $LaSrFe_{0.5}Rh_{0.5}O_3$ which is consistent with the presence of Rh^{4+} in both cases.

of 100 Oe (Fig. 5) diverge weekly below 100 K, before diverging more strongly below 60 K, consistent with the onset of magnetic order. Data in the range $100 < T/K < 300$ do not obey the Curie–Weiss law. Magnetization-field data collected at 5 K are consistent with ferromagnetic behaviour with a coercive field of 190 Oe (as shown more clearly in Fig. S3 in the ESI†) and a saturated moment of $1.43\mu_B$ per formula unit ($2.86\mu_B$ per Mn).

Temperature-dependent 4-probe transport measurements indicate that $La_{0.5}Sr_{0.5}Mn_{0.5}Rh_{0.5}O_3$ is highly resistive, with a semiconducting/insulating temperature dependence ($\delta\rho/\delta T < 0$) as shown in Fig. 6. A plot of $\ln\rho$ against $T^{-1/4}$ is linear in the range $90 < T/K < 300$ consistent with 3D variable range hopping.

Magnetic characterisation of $La_{0.5}Sr_{0.5}Fe_{0.5}Rh_{0.5}O_3$

ZFC and FC data collected from $La_{0.5}Sr_{0.5}Fe_{0.5}Rh_{0.5}O_3$ (Fig. 7) can be fit by the Curie–Weiss law ($\chi = C/(T - \theta) + K$) in the temperature range $60 < T/K < 300$ to yield value of $C = 1.132(1)$
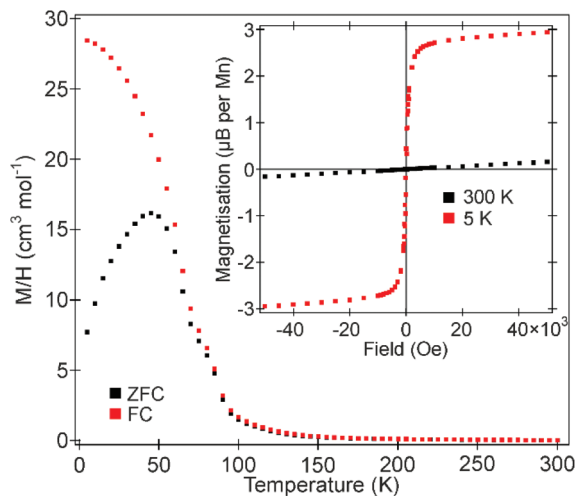
Paper

Fig. 5 ZFC and FC magnetisation data collected from $La_{0.5}Sr_{0.5}Mn_{0.5}Rh_{0.5}O_3$ in an applied field of 100 Oe. Inset shows magnetisation-field isotherms collected at 300 K and 5 K.

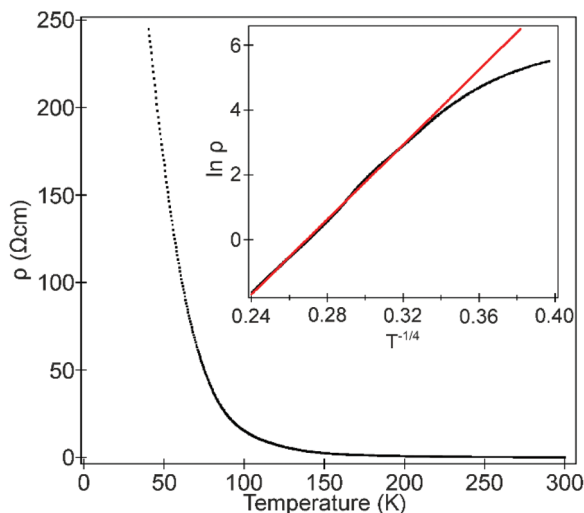**Fig. 6** Temperature-dependent resistivity of $La_{0.5}Sr_{0.5}Mn_{0.5}Rh_{0.5}O_3$. Inset shows fit to 3D variable-range hopping model.

Fig. 7 (Top) ZFC and FC magnetisation data collected from $La_{0.5}Sr_{0.5}Fe_{0.5}Rh_{0.5}O_3$ in an applied field of 100 Oe. Inset shows Curie–Weiss law fit to the ZFC data. (Bottom) Magnetisation-field isotherms collected from $La_{0.5}Sr_{0.5}Fe_{0.5}Rh_{0.5}O_3$ at 300 K and at 5 K after field cooling from 300 K in an applied filed of 50 000 Oe.

cm^3 K mol^{-1}, $\theta = -30.9$ K, $K = 7.75(7) \times 10^{-4}$ cm^3 mol^{-1}, as shown in Fig. 6. For $T < 45$ K the ZFC and FC data diverge, indicative of a magnetic phase transition. Magnetization data collected at 300 K exhibit a linear field dependence. In contrast, magnetization data collected at 5 K after cooling from 300 K in an applied field of 50 000 Oe exhibit hysteresis and are displaced from the origin, indicative of spin-glass behaviour.

Temperature-dependent 4-probe transport measurements indicate that $La_{0.5}Sr_{0.5}Fe_{0.5}Rh_{0.5}O_3$ is highly resistive, with a semiconducting/insulating temperature dependence ($\delta\rho/\delta T < 0$) as shown in Fig. 8. A plot of $\ln \rho$ against $T^{-1/4}$ is linear in the range $50 < T/K < 300$ consistent with 3D variable range hopping.
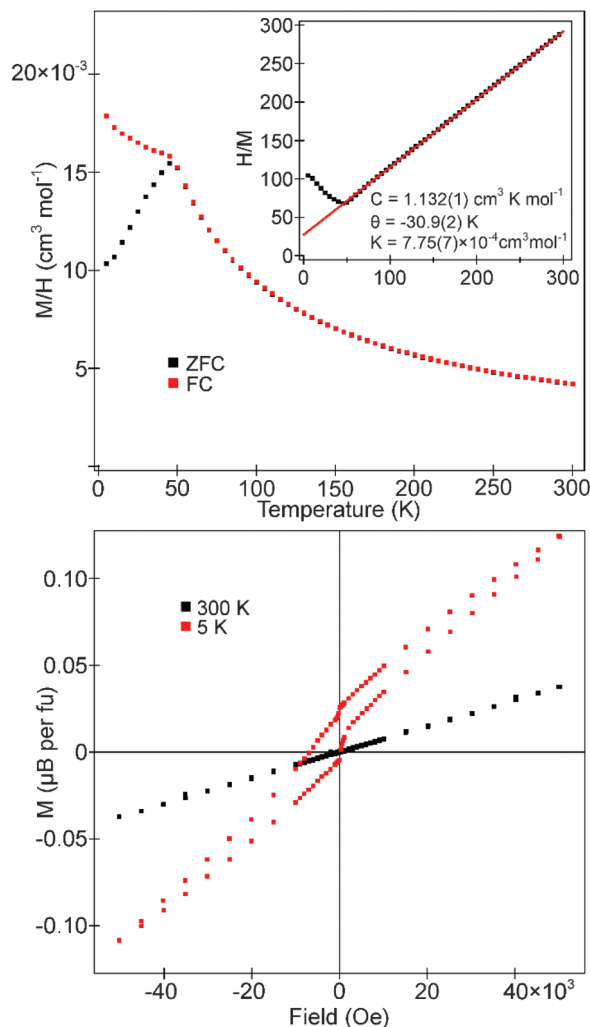
Discussion

SXRD data indicate that in common with other reported $La_{1-x}Sr_xMn_{0.5}Rh_{0.5}O_3$ phases,[15,29] $La_{0.5}Sr_{0.5}Mn_{0.5}Rh_{0.5}O_3$ adopts a cation-disordered, $a^-a^-c^+$ distorted, $GdFeO_3$-type perovskite structure. Comparison with the reported structures of $LaMn_{0.5}Rh_{0.5}O_3$ and $La_{0.75}Sr_{0.25}Mn_{0.5}Rh_{0.5}O_3$ reveals that both the unit cell volumes ($V = 243.92$ $Å^3$, 240.01 $Å^3$ and 236.08 $Å^3$ for $x = 0$, 0.25 and 0.5 respectively) and average (Mn/Rh)–O bond lengths ((Mn/Rh)–O = 2.019 Å, 1.995 Å and 1.971 Å for $x = 0$, 0.25 and 0.5 respectively) decrease on substitution of La^{3+} by Sr^{2+}, consistent with oxidation of the transition metal cations. In addition it should be noted that there is no evidence of an ordered Jahn–Teller distortion (long-range orbital order) of the $(Mn/Rh)O_6$ octahedra in $La_{0.5}Sr_{0.5}Mn_{0.5}Rh_{0.5}O_3$ (Table 2) or any other $La_{1-x}Sr_xMn_{0.5}Rh_{0.5}O_3$ phases (despite

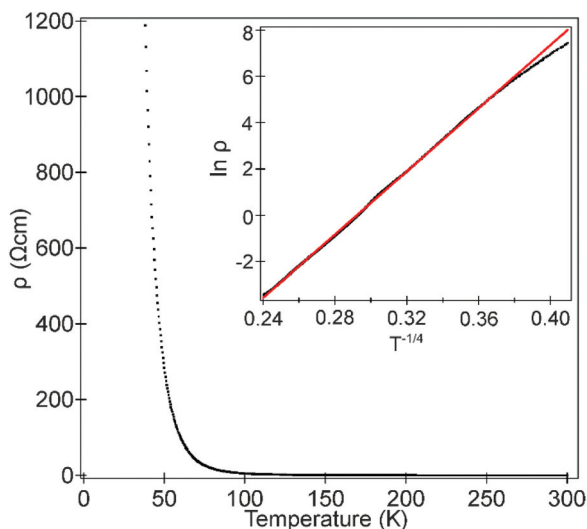**Fig. 8** Temperature-dependent resistivity of $La_{0.5}Sr_{0.5}Fe_{0.5}Rh_{0.5}O_3$. Inset shows fit to 3D variable-range hopping model.

the unambiguous presence of Mn^{3+} in $LaMn_{0.5}Rh_{0.5}O_3$[15] which is attributed to suppression by the disordered arrangement of the Mn and Rh cations.

$La_{0.5}Sr_{0.5}Fe_{0.5}Rh_{0.5}O_3$ also adopts a cation-disordered, $a^-a^-c^+$ distorted, $GdFeO_3$-type perovskite structure. Comparison with the reported structure of $LaFe_{0.5}Rh_{0.5}O_3$[13] again reveals that substitution of La^{3+} with Sr^{2+} leads to a contraction in unit cell volume, consistent with oxidation of the transition metals.

XPS and ^{57}Fe Mössbauer data indicate the predominant oxidation state combinations of $La_{0.5}Sr_{0.5}Mn_{0.5}Rh_{0.5}O_3$ and $La_{0.5}Sr_{0.5}Fe_{0.5}Rh_{0.5}O_3$ are Mn^{3+}/Rh^{4+} and Fe^{3+}/Rh^{4+} respectively. This is unexpected considering the oxide chemistry of these transition metals. For example, Mn^{3+} is not particularly stable in perovskite oxides, as illustrated by the observation that $LaMnO_3$ must be prepared under low oxygen partial pressures to avoid the formation of mixed-valent $Mn^{3+/4+}$ '$LaMnO_{3+\delta}$' phases.[30] In contrast the preparation of Mn^{4+} containing perovskite oxides, such as $SrMnO_3$, can be readily achieved by heating in air.[31] Rhodium shows the opposite trend with Rh^{3+} perovskites such as $LaRhO_3$ being readily prepared in air,[32] while Rh^{4+} perovskite oxides such as $SrRhO_3$ require high-pressure synthesis conditions.[33] It is therefore surprising that combining the two 'more stable' perovskite phases $LaRhO_3$ and $SrMnO_3$ to form $La_{0.5}Sr_{0.5}Mn_{0.5}Rh_{0.5}O_3$ leads to a change in oxidation states from a Mn^{4+}/Rh^{3+} combination in the ternary phases to a Mn^{3+}/Rh^{4+} in the quaternary product. Rh^{4+} has been observed in perovskite oxides prepared at ambient pressure when it is combined with either electronegative elements such as Cu ($LaCu_{0.5}^{2+}Rh_{0.5}^{4+}O_3$)[15] or elements which only exhibit a single divalent cation oxidation state ($LaZn_{0.5}^{2+}Rh_{0.5}^{4+}O_3$, $LaMg_{0.5}^{2+}Rh_{0.5}^{4+}O_3$).[34] However, the observation of Rh^{4+} in the presence of cations such as Fe^{3+} and Mn^{3+} which can be oxidized relatively easily is unexpected and

suggests the 3d and 4d levels of Mn/Fe and Rh respectively are of similar energy.

Magnetic behaviour

Transport and magnetization data indicate that $La_{0.5}Sr_{0.5}Mn_{0.5}Rh_{0.5}O_3$ is an electrical insulator which undergoes a transition to a ferromagnetic state at $T_c \sim 60$ K. This behaviour is very similar to that reported for other perovskite oxides containing disordered arrays of Mn^{3+} cations such as $LaMn_{0.5}Rh_{0.5}O_3$ ($T_c = 65$ K)[15,16] and $LaMn_{0.5}Ga_{0.5}O_3$ ($T_c = 70$ K), with the observed saturated ferromagnetic moment of $La_{0.5}Sr_{0.5}Mn_{0.5}Rh_{0.5}O_3$ ($2.86\mu_B$ per Mn) also being similar to that observed for $LaMn_{0.5}Ga_{0.5}O_3$.[35,36]

The ferromagnetic behaviour of $LaMn_{0.5}Ga_{0.5}O_3$ has been rationalized by observing that partial substitution of the Mn^{3+} cations in $LaMnO_3$ by a non-Jahn–Teller ion (e.g. Ga^{3+}) suppresses the static Jahn–Teller distortion (orbital ordering) of the $Mn^{III}O_6$ units present in the unsubstituted phase.[35,37] In the absence of a static Jahn–Teller distortion (long-range orbital order), local dynamic Jahn–Teller distortions predominate which make all the Mn–O–Mn exchange couplings ferromagnetic, thus explaining the ferromagnetic order observed for $LaMn_{1-x}Ga_xO_3$ phases with $x > 0.5$.[35,37] This mechanism can also be invoked to explain the ferromagnetic behaviour of $LaMn_{0.5}Rh_{0.5}O_3$ as it is observed that the substitution of diamagnetic, low-spin d^6, Rh^{3+} into $LaMnO_3$ suppresses the static Jahn–Teller distortion of the $Mn^{III}O_6$ units in a manner directly analogous to Ga^{3+} substitution.[15,38]

We propose that this dynamic Jahn–Teller mechanism is also the origin of the ferromagnetic behaviour of $La_{0.5}Sr_{0.5}Mn_{0.5}Rh_{0.5}O_3$, as the substitution of Rh^{4+} for Mn^{3+} suppresses the static Jahn–Teller distortion of the manganese centres, leading to ferromagnetic couplings between Mn^{3+} cations in this cation-disordered material. It may be expected that the presence of paramagnetic Rh^{4+} centres would perturb the ferromagnetic Mn–O–Mn couplings, however the observation that the Curie temperature of $La_{0.5}Sr_{0.5}Mn_{0.5}Rh_{0.5}O_3$ ($T_c \sim 60$ K) is very similar to those of $LaMn_{0.5}Rh_{0.5}O_3$ ($T_c = 65$ K)[15,16] and $LaMn_{0.5}Ga_{0.5}O_3$ ($T_c = 70$ K)[35,36] indicates any Mn–O–Rh couplings present are weak. It is not clear if the Rh spins contribute to the magnetically ordered state of $La_{0.5}Sr_{0.5}Mn_{0.5}Rh_{0.5}O_3$.

Magnetization data collected from $La_{0.5}Sr_{0.5}Fe_{0.5}Rh_{0.5}O_3$ in the temperature range $60 < T/K < 300$ exhibit the temperature-dependence of the Curie–Weiss Law (Fig. 6). However, the Curie constant extracted from these data ($C = 1.132(1)$ cm^3 K mol^{-1}) is much smaller than expected for simple paramagnetic behaviour for either an Fe^{3+}/Rh^{4+} ($C_{expected} = 2.375$ cm^3 K mol^{-1}) or an Fe^{4+}/Rh^{3+} ($C_{expected} = 1.50$ cm^3 K mol^{-1}) oxidation state combination. This indicates that strong spin–spin interactions are present in this temperature range, which is consistent with the large temperature-independent susceptibility observed ($K = 7.75(7) \times 10^{-4}$ cm^3 mol^{-1}) which contributes ~20% to the total susceptibility at 300 K.

On cooling below $T = 45$ K, $La_{0.5}Sr_{0.5}Fe_{0.5}Rh_{0.5}O_3$ undergoes a transition to a spin-glass state. In order to adopt a spin-glass

state a system must be crystallographically disordered, and subject to magnetic frustration. If we consider the nearest-neighbour super exchange couplings in $La_{0.5}Sr_{0.5}Fe_{0.5}Rh_{0.5}O_3$ we observe Fe^{III}–O–Fe^{III} should be strongly antiferromagnetic, Rh^{IV}–O–Rh^{IV} should also be antiferromagnetic, but only weakly, and Fe^{III}–O–Rh^{IV} should be ferromagnetic.[8] If these are the only significant magnetic couplings, a disordered Fe/Rh array would not be subject to magnetic frustration, making the observed spin-glass behaviour of $La_{0.5}Sr_{0.5}Fe_{0.5}Rh_{0.5}O_3$ a little puzzling.

Battle *et al.* considered the spin-glass states of $SrFe_{0.5}Ru_{0.5}O_3$ and $Sr_2Fe_{0.5}Ru_{0.5}O_4$ which arise from disordered arrays of Fe^{3+} and Ru^{5+}.[39,40] The nearest-neighbour super exchange couplings in $SrFe_{0.5}Ru_{0.5}O_3$ and $Sr_2Fe_{0.5}Ru_{0.5}O_4$ are directly analogous to those in $La_{0.5}Sr_{0.5}Fe_{0.5}Rh_{0.5}O_3$: Fe^{III}–O–Fe^{III} is antiferromagnetic, Ru^V–O–Ru^V is antiferromagnetic and Fe^{III}–O–Ru^V is ferromagnetic.

Battle *et al.* concluded that the order of coupling strengths is Fe^{III}–O–Fe^{III} > Ru^V–O–Ru^V ~ Fe^{III}–O–Ru^V ~ Fe^{III}–O–O–Fe^{III} where this last term is the next-nearest-neighbour Fe–Fe coupling. In this situation, frustration arises because the ferromagnetic Fe^{III}–O–Ru^V couplings align next-nearest neighbour Fe spins ferromagnetically, but the Fe^{III}–O–O–Fe^{III} super–super exchange coupling is antiferromagnetic and the two couplings have about the same strength. We propose that a similar frustration between nearest-neighbour Fe^{III}–O–Rh^{IV} and next-nearest-neighbour Fe^{III}–O–O–Fe^{III} couplings is responsible for the spin-glass behaviour in $La_{0.5}Sr_{0.5}Fe_{0.5}Rh_{0.5}O_3$.

It is interesting to note that the contrasting magnetic behaviour of $La_{0.5}Sr_{0.5}Mn_{0.5}Rh_{0.5}O_3$ and $La_{0.5}Sr_{0.5}Fe_{0.5}Rh_{0.5}O_3$ can be understood on the basis of the relative strengths of the different transition-metal couplings in the two systems – the dominance of 3d–3d couplings in $La_{0.5}Sr_{0.5}Mn_{0.5}Rh_{0.5}O_3$ leading to ferromagnetism; the comparable strengths of 3d–3d, 3d–4d couplings in $La_{0.5}Sr_{0.5}Fe_{0.5}Rh_{0.5}O_3$ resulting in spin-glass behaviour.

Conclusions

Hole doping of the perovskite phases $LaMn_{0.5}Rh_{0.5}O_3$ and $LaFe_{0.5}Rh_{0.5}O_3$ leads to the oxidation of Rh^{3+} to Rh^{4+} in the resulting $La_{0.5}Sr_{0.5}Mn_{0.5}Rh_{0.5}O_3$ and $La_{0.5}Sr_{0.5}Fe_{0.5}Rh_{0.5}O_3$ compounds. The stabilization of Rh^{4+} in the presence of the readily oxidizable Mn^{3+} and Fe^{3+} cations suggests that the 3d Mn/Fe states and 4d Rh states are of similar energy, so that if the electronic bandwidth of the phases could be increased, by decreasing the magnitude of the octahedral tilting distortion for example, or the 3d and 4d cations could be ordered, correlated electronic behaviour is likely, in line with computational predictions for high-valent rhodium oxides.[41]

Conflicts of interest

There are no conflicts to declare.

Acknowledgements

Notes and references

1 R. J. D. Tilley, *Perovskites: Structure-Property Relationships*, John Wiley and Sons, Chichester, 2016.
2 J. B. Goodenough and J.-S. Zhou, *Chem. Mater.*, 1998, **10**, 2980–2993.
3 T. Saha-Dasgupta, *Mater. Res. Express*, 2020, **7**, 014003.
4 A. Halder, P. Sanyal and T. Saha-Dasgupta, *Phys. Rev. B*, 2019, **99**, 020402(R).
5 K. L. Kobayashi, T. Kimura, H. Sawada, K. Terakura and Y. Tokura, *Nature*, 1998, **395**, 677–680.
6 K. I. Kobayashi, T. Kimura, Y. Tomioka, H. Sawada, K. Terakura and Y. Tokura, *Phys. Rev. B: Condens. Matter Mater. Phys.*, 1999, **59**, 11159–11162.
7 H. Kato, T. Okuda, Y. Okimoto, Y. Tomioka, Y. Takenoya, A. Ohkubo, M. Kawasaki and Y. Tokura, *Appl. Phys. Lett.*, 2002, **81**, 328–330.
8 J. B. Goodenough, *Magnetism and the chemical bond*, Wiley, New York, 1963.
9 S. Kanungo, B. H. Yan, M. Jansen and C. Felser, *Phys. Rev. B: Condens. Matter Mater. Phys.*, 2014, **89**, 214414.
10 X. D. Ou, Z. W. Li, F. R. Fan, H. B. Wang and H. Wu, *Sci. Rep.*, 2014, **4**(7542), 7541–7544.
11 R. Morrow, M. A. McGuire, J. Q. Yan and P. M. Woodward, *Inorg. Chem.*, 2018, **57**, 2989–3001.
12 S. Vasala and M. Karppinen, *Prog. Solid State Chem.*, 2015, **43**, 1–36.
13 A. E. Smith, A. W. Sleight and M. A. Subramanian, *Mater. Res. Bull.*, 2010, **45**, 460–463.
14 P. D. Battle and J. F. Vente, *J. Solid State Chem.*, 1999, **146**, 163–167.
15 J. Ting, B. J. Kennedy, Z. Zhang, M. Avdeev, B. Johannessen and L. Y. Jang, *Chem. Mater.*, 2010, **22**, 1640–1646.
16 C. Schinzer, *J. Phys. Chem. Solids*, 2000, **61**, 1543–1551.
17 K. Knizek, J. Hejtmanek, M. Marysko, Z. Jirak and J. Bursik, *Phys. Rev. B*, 2012, **85**, 134401.
18 J. Li, A. E. Smith, K. S. Kwong, C. Powell, A. W. Sleight and M. A. Subramanian, *J. Solid State Chem.*, 2010, **183**, 1388–1393.
19 S. V. Streltsov, V. V. Gapontsev and D. I. Khomskii, *J. Phys.: Condens. Matter*, 2016, **28**, 086005.
20 A. C. Larson and R. B. Von Dreele, Los Alamos National Laboratory Report LAUR 86-748, 2000.

21 K. Lagarec and D. G. Rancourt, *Recoil: Mössbauer spectral analysis software for windows*, 1998.

22 J. P. Hodges, S. Short, J. D. Jorgensen, X. Xiong, B. Dabrowski, S. M. Mini and C. W. Kimball, *J. Solid State Chem.*, 2000, **151**, 190–209.

23 Y. Takeda, K. Kanno, T. Takada, O. Yamamoto, M. Takano, N. Nakayama and Y. Bando, *J. Solid State Chem.*, 1986, **63**, 237–249.

24 E. N. K. Glover, S. G. Ellington, G. Sankar and R. G. Palgrave, *J. Mater. Chem. A*, 2016, **4**, 6946–6954.

25 T. K. Le, D. Flahaut, H. Martinez, N. Andreu, D. Gonbeau, E. Pachoud, D. Pelloquin and A. Maignan, *J. Solid State Chem.*, 2011, **184**, 2387–2392.

26 M. C. Biesinger, B. P. Payne, A. P. Grosvenor, L. W. M. Lau, A. R. Gerson and R. S. Smart, *Appl. Surf. Sci.*, 2011, **257**, 2717–2730.

27 T. Yamashita and P. Hayes, *Appl. Surf. Sci.*, 2008, **254**, 2441–2449.

28 E. S. Ilton, J. E. Post, P. J. Heaney, F. T. Ling and S. N. Kerisit, *Appl. Surf. Sci.*, 2016, **366**, 475–485.

29 B. Bakowski, P. D. Battle, E. J. Cussen, L. D. Noailles, M. J. Rosseinsky, A. I. Coldea and J. Singleton, *Chem. Commun.*, 1999, 2209–2210.

30 N. Kamegashira, Y. Miyazaki and H. Yamamoto, *Mater. Chem. Phys.*, 1984, **11**, 187–194.

31 K. Kuroda, K. Shinozaki, K. Uematsu, N. Mizutani and M. Kato, *J. Am. Ceram. Soc.*, 1980, **63**, 109–110.

32 H. J. Gysling, J. R. Monnier and G. Apai, *J. Catal.*, 1987, **103**, 407–418.

33 K. Yamaura and E. Takayama-Muromachi, *Phys. Rev. B*, 2001, **64**, 224424.

34 C. Schinzer and G. Demazeau, *J. Mater. Sci.*, 1999, **34**, 251–256.

35 J. Blasco, J. Garcia, J. Campo, M. C. Sanchez and G. Subias, *Phys. Rev. B*, 2002, **66**, 174431.

36 E. J. Cussen, M. J. Rosseinsky, P. D. Battle, J. C. Burley, L. E. Spring, J. F. Vente, S. J. Blundell, A. I. Coldea and J. Singleton, *J. Am. Chem. Soc.*, 2001, **123**, 1111–1122.

37 J. Goodenough, R. J. Arnott, N. Menyuk and A. Wold, *Phys. Rev.*, 1961, **124**, 373–384.

38 M. T. Haque, H. Satoh and N. Kamegashira, *J. Alloys Compd*, 2005, **390**, 115–121.

39 P. D. Battle, T. C. Gibb, C. W. Jones and F. Studer, *J. Solid State Chem.*, 1989, **78**, 281–293.

40 P. D. Battle, S. K. Bollen and A. V. Powell, *J. Solid State Chem.*, 1992, **99**, 267–275.

41 A. Halder, D. Nafday, P. Sanyal and T. Saha-Dasgupta, *npj Quantum Mater.*, 2018, **3**, 17.